optica

Superresolution imaging of the local density of states in plasmon lattices

Ke Guo,[1] Marc A. Verschuuren,[2] and A. Femius Koenderink[1,*]

[1]Center for Nanophotonics, FOM Institute AMOLF, Science Park 104, 1098 XG Amsterdam, The Netherlands
[2]Philips Research Laboratories, High Tech Campus 4, 5656 AE Eindhoven, The Netherlands
*Corresponding author: f.koenderink@amolf.nl

Received 20 November 2015; revised 15 February 2016; accepted 15 February 2016 (Doc. ID 254237); published 11 March 2016

Periodic plasmonic nanostructures have been found promising in controlling photoluminescence directivity and efficiency for a wide variety of applications. Because of the inhomogeneous spatial distribution of the photonic resonances of periodic plasmonic nanostructures, their influence on emission is strongly dependent on the position of emitters relative to the nanostructures. Therefore, mapping the local dependence of directivity, efficiency, and emission rate enhancements is key to understanding and optimizing the devices. We introduce a method of mapping the local enhancement of spontaneous emission rates of emitters coupled to periodic nanostructures based on stochastic superresolution imaging. As an example, we show superresolved measurements of the local density of states (LDOS) at 605 nm induced by a hexagonal lattice of aluminum nanoantennas with a spatial resolution of 40 nm, defined by the size of the colloidal nanosources we use as randomly dispersed probes. We demonstrate that our method is superior to near-field mapping of emission rates. Comparison with electrodynamic simulations indicates that the variation of the decay rate of the emitters in the investigated sample is hardly influenced by the lattice modes and mainly governed by single-particle LDOS variations and nearest-neighbor interactions.

OCIS codes: (180.2520) Fluorescence microscopy; (250.5403) Plasmonics; (250.5230) Photoluminescence.

http://dx.doi.org/10.1364/OPTICA.3.000289

1. INTRODUCTION

Collective electron excitations in plasmonic nanostructures, known as localized surface plasmon resonances (LSPRs), enable the manipulation of photoluminescence at the nanoscale [1–5]. The underlying physics is that plasmonic nanostructures support optical resonances that are associated with very strong scattering cross sections, large optical polarizabilities, and strong electromagnetic near fields, because many electrons contribute [6,7]. Coupling these optical resonances to emitters enhances the absorption of pump light by emitters, allows their radiation to be redirected in preferred directions, and gives rise to emission rate enhancements, due to enhanced local density of states (LDOS) effects [1,2]. Moreover, periodic plasmonic nanostructures, particularly arrays of plasmonic nanoantennas [8], can support lattice modes that are delocalized. These modes can couple to emitters in a much broader range of distances than just the nanometer vicinity of the metal particles. Consequently, they are well suited to enhance emission of ensembles of fluorophores, and have been found promising in applications such as solid-state lighting [9–11], lasing [12–15], photovoltaics [16–19], surface-enhanced Raman spectroscopy [20–23], and sensing [24,25].

Due to the inhomogeneous spatial distribution of the photonic–plasmonic resonances of periodic plasmonic nanostructures, their influence on emission enhancement can depend strongly on the position of emitters relative to the nanostructures. [1,2,26–28] Therefore, mapping the local dependence of emission rates, efficiency, and directivity is key to optimizing the relevant plasmon-enhanced light-emitting devices. Indeed, enhanced LDOS effects are frequently measured by fluorescence lifetime measurements to characterize the influence of nanostructures on emission efficiency enhancements [2,26–29]. Also, Fourier images [30] are frequently measured to characterize the influence of nanostructures on emitter directivity. However, to date, these methods have been applied mainly on the level of ensembles of emitters, without spatial resolution in the unit cell. Since unit cells are typically wavelength sized, and plasmon near fields have spatial features on the scale of 10–50 nm, mapping as a function of fluorophore position is highly challenging. Conventional diffraction-limited optical microscopes enable optical measurements at the scale of the wavelength but are insufficient for studying local optical properties of nanostructures with subwavelength resolution.

Superresolution techniques such as near-field scanning optical microscopy (NSOM) [31] using scanning probes have been employed to the study of nanostructures to overcome the diffraction limit. Several groups have pursued scanning emitter microscopy, where the scanning probe is a single fluorophore attached to a sharp tip, such as an atomic force microscopy probe, or a glass fiber tapered to nanometric size [1,2,4,5,26,27,32–39]. These

techniques use fragile scanning tips and, therefore, require accurate feedback systems, and carry a high risk of failure due to tip breakage. Moreover, since tips are scanned over the surfaces of the samples, measurements are limited to those surfaces and can be affected by topological artifacts. An alternative approach to *scanning* the source to obtain an image is to use selective positioning of single nanoprobes on many identical nanostructures for measurement with subwavelength resolution. This could be arranged by lithographically attaching nano-emitters [40,41] in the nanostructure during sample fabrication, or alternatively by pushing nanoprobes using nanopositioning techniques, such as atomic force microscopy [3,42–44]. These methods typically require advanced nanofabrication or nanopositioning techniques. Measurements on nanoprobes randomly casted on nanostructures have also been conducted [28,29]. However, since the nanoprobes are immobile and isolated in space, it is impossible to measure on two positions closer than the diffraction limit and, therefore, the measurements do not result in complete maps. Another state-of-the-art superresolution technique is photoactivation localization microscopy (PALM), or stochastic optical reconstruction microscopy (STORM), which has revolutionized fluorescence microscopy, as recognized by the 2014 Nobel Prize in Chemistry [45–47]. While localization microscopy is usually used to map spatial distributions of molecules in biophysical systems, it can also be used to map other quantities. Indeed, superresolution localization microscopy has already been utilized to characterize the local field enhancement of plasmonic nanostructures. Superresolution on single structures was achieved by isolating nanoprobes with temporal photoactivation [48] or using (slow) diffusion in an immersion liquid [49–53] and retrieving the positions of the nanoprobes by fitting snapshot fluorescent images with the point spread function (PSF). Such a photoactivation approach requires very particular fluorophores, while using diffusion assumes particular solvents that, in turn, limit the dielectric environment of the system being imaged.

In this article, we demonstrate a simple stochastic superresolution technique for mapping of the LDOS from periodic plasmonic nanostructures using randomly deposited nanoprobes that is not subject to the aforementioned limitations. For periodic nanostructures, since any one position in the unit cell is replicated in all other unit cells, measurement results from different unit cells are combined to construct a map of the primitive unit cell. The method is applied to determining a map of the LDOS of a hexagonal array of aluminum nanoantennas, which has previously been shown to be highly effective for solid-state lighting [11]. We obtain a spatial resolution of 40 nm (at 605 nm wavelength), defined by the size of the nanoprobes used in the measurement. We compare the data to measurements on the same array with a scanning-excitation technique based on NSOM. This comparison reveals that superresolution imaging is advantageous in simplicity of operation, required infrastructure, and fidelity, since it does not suffer from the topography artifacts of NSOM. Finally, we use FDTD simulations to understand the observed LDOS variations. We show that the variation of the decay rate of the emitters in the investigated sample is hardly influenced by the lattice modes and governed mainly by single-particle LDOS variations and nearest-neighbor couplings.

2. DESIGN CONSIDERATIONS FOR THE EXPERIMENTAL METHOD

Our approach to stochastic superresolution imaging of LDOS in periodic systems is to randomly distribute single nanoprobes over a large sample area containing many unit cells. The proposed experimental method then requires two major steps: (i) localization, i.e., determination of the position of the nanoprobes and the nanostructure with subdiffraction limited accuracy and (ii) optical measurements on individual nanoprobes quantifying LDOS, i.e., fluorescence lifetime. Relevant questions regarding the first step are, first, how accurately can one localize a nanoprobe and the plasmonic lattice, and second, how many nanoprobes does one need to measure for an accurate probing of the unit cell.

Regarding localization, the position of a nanoprobe relative to the nanostructure can be determined from a combination of a fluorescence image of the nanoprobes that does not show the plasmon lattice, and a white-light reflection image of the nanostructure that does not show the nanoprobe, provided the two images can be acquired without relative shift. The absolute position of a nanoprobe in a fluorescent image can be accurately obtained as the centroid of its fluorescence image, i.e., a diffraction-limited spot. The accuracy of this localization is then determined by the diffraction limit and the signal-to-noise ratio (SNR), which could reach a few nanometers given high SNR [54]. The unit cell of the nanostructure near the nanoprobe is identified from a reflection image measured with the very same optical path (including using the same microscope filter set) as the fluorescence measurement.

Optical measurements are done in a confocal measurement scheme to allow fluorescence lifetime measurements of individual nanoprobes. Important questions are how must the nanoprobes be distributed, and how many need to be sampled. Clearly the separation of the nanoprobes must exceed the diffraction limit so that they are resolvable in the fluorescence image and to avoid excitation of multiple nanoprobes simultaneously. We thus require a dilute sprinkling of fewer than one nanoprobe per square micrometer. By repeating the position determination and optical measurements on a number of nanoprobes, we will obtain the dependence of the measured lifetime on the position in the primitive cell. To construct a complete map, the nanoprobes need to be ergodically distributed on the periodic nanostructure. The resolution and completeness of the map will depend on the number of measured nanoprobes. First, for a given target sampling density or "pixel size," one can ask how many probes are required so that the chance of all pixels having a nanoprobe is near-unity. Second, averaging the results from different nanoprobes at similar positions in the primitive cell helps to reduce the statistical error due to (i) the statistical error in the optical measurements and (ii) differences between different nanoprobes (iii) and differences between unit cells of the nanostructure.

Here we estimate the number of nanoprobes to be measured for a statistically significant map. Assuming a primitive cell with an area of A_{map} divided into a square grid of sampling pixels, for each grid point we calculate the average of the measured LDOS of nanoprobes in an area of Δ_A around the grid point, where Δ_A can be chosen on the basis of the grid spacing, or on the basis of the accuracy of the localization. The probability that at least M out of N_{probe} measured nanoprobes fall into Δ_A around a given grid point is

$$P(M;N_{\mathrm{probe}}) = 1 - \sum_{i=0}^{M-1} \binom{i}{N_{\mathrm{probe}}} \left(\frac{\Delta_A}{A_{\mathrm{map}}}\right)^i \left(1 - \frac{\Delta_A}{A_{\mathrm{map}}}\right)^{N_{\mathrm{probe}}-i}. \quad (1)$$

This probability is close to unity as long as $N_{probe} \gg M, A_{map}/\Delta_A$.

For a map, one would at least require $M = 1$ for all pixels (no empty pixel), setting a minimum required N_{probe}. Furthermore it is advantageous to require $M > 1$ so that averages of optical observables can be determined for a more accurate map. To have an idea about how to choose N_{probe} for given target M, we performed a numerical experiment. By way of example we consider a hexagonal plasmonic lattice with a pitch of 550 nm relevant for solid-state lighting that contains particles with a rounded square base, as we study in the experiment below. All information about this structure (for scalar quantities) is contained in one-fourth of the primitive unit cell, leading to an area $A_{map} \approx 6.5 \times 10^4$ nm^2 that requires mapping. In our work we will use 40 nm sized beads as nanoprobes, which we assume as a bound for the accuracy of the localization and, thereby, define area $\Delta_A \approx 1.3 \times 10^3$ nm^2 in our example. Typically, to obtain accurate spatial maps one would oversample compared to the resolution. In this example, we assume that we sample the map at 10 nm grid spacing, leading to ~650 grid points. Figure 1(b) shows an averaged histogram obtained from 1000 Monte Carlo experiments with different N_{probe}, where n_{grid} is the (average) number of grid points that receive n_{probe} nanoprobes in their vicinity of Δ_A, and particles are assumed to be deposited with uniform, uncorrelated probability.

Measuring 600 nanoprobes is enough for constructing a rough map, in the sense that all the pixels are expected to receive at least one nanoprobe ($n_{grid}(n_{probe} = 0) = 0$). With 1000 nanoprobes, almost all of the pixels have at least four nanoprobes ($n_{grid}(n_{probe} < 4) < 1$), meaning a reduction of statistical errors in the observable by a factor of 2, assuming normally distributed errors in the observable.

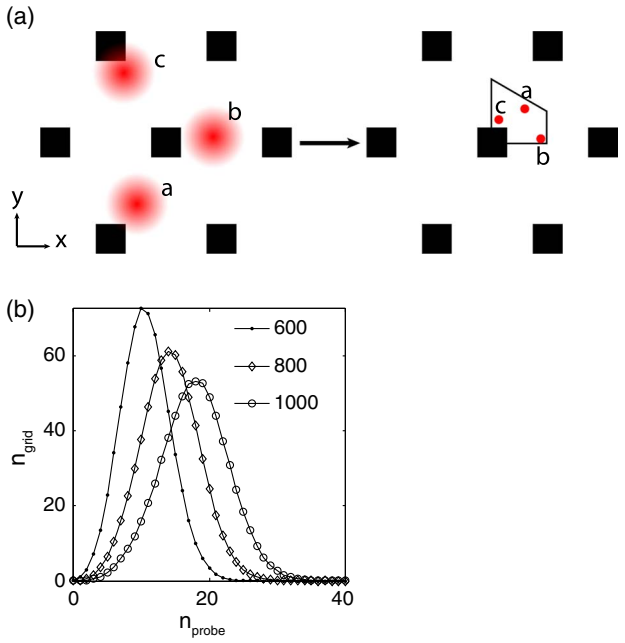

Fig. 1. (a) Schematic of the superresolution method applied on a hexagonal array of nanoantennas. Nanoprobes randomly deposited on the sample are measured with their positions determined as the centroids of their fluorescence images. The measurement results are translated into one primitive cell of the sample to construct a map. (b) Histograms showing distribution of probes obtained from Monte Carlo experiments. n_{grid} is the average number of grid points that have n_{probe} nanoprobes falling into each of the averaging area (Δ_A) with the total number of probes (N_{probe}) indicated in the legend.

3. REALIZATION OF THE METHOD

We apply the method to a plasmonic nanostructure that is a hexagonal array of Al nanoantennas with a lattice constant of $d = 550$ nm. This type of plasmonic nanostructure has been demonstrated to exhibit lattice resonances that are able to couple light into defined directions and are therefore beneficial for improving LED-pumped remote phosphors in solid-state lighting systems [11]. Apart from enhanced brightness due to outcoupling in particular desired angular ranges, enhancement in the absorption of pump light and in the fluorescence quantum yield of emitters due to LDOS enhancement can also contribute to the enhancement of light emission. Thus, it is unclear whether the reported [11] directional brightness enhancement is actually accompanied by an increased or decreased LDOS and, hence, by an increased or decreased internal quantum efficiency. The distribution of the LDOS of such nanostructure has not been mapped and the contribution of the lattice modes to the LDOS enhancement is unknown. A scanning electron microscope (SEM) image of the array is shown in Fig. 2(a). The array of Al nanoantennas is fabricated over an area of ~5 mm × 5 mm on a fused silica glass substrate by combining substrate conformal imprint lithography with reactive ion etching. [11,55] Each nanoantenna is shaped like a nanocone with a height of 150 nm and a rounded square section with a lateral size of 80 nm at the top and 140 nm at the base, which introduces asymmetry in forward–backward emission and is suited for solid-state lighting [56]. Spherical polystyrene particles with a diameter of 40 nm loaded with fluorescent dye molecules are used as nanoprobes. They absorb green light and emit around 605 nm [Invitrogen FluoSpheres, product number F-8793]. On top of the array an ~30 nm polystyrene layer is spin-coated to provide a hydrophobic surface for protection of the Al nanoantennas from corrosive degradation and, meanwhile, to make it easier to sparsely deposit the nanoprobes and avoid clustering. A drop of a 0.02 mM suspension of nanoprobes in water is dropped over the sample and slowly blown away with a pressurized air gun. Repeating the process multiple times, we are able to attach the nanoprobes randomly on the surface of the sample with a density of $\rho_{probe} \sim 0.15$ μm^{-2}. Compared with classical spin coating, this method requires much lower probe concentration and, therefore, is much less wasteful.

The experimental setup is based on a confocal microscope, the schematic of which is shown in Fig. 2(b). A pulsed laser with a wavelength of 532 nm and a repetition rate of 10 MHz is used to excite the nanoprobes for the fluorescence measurements. For

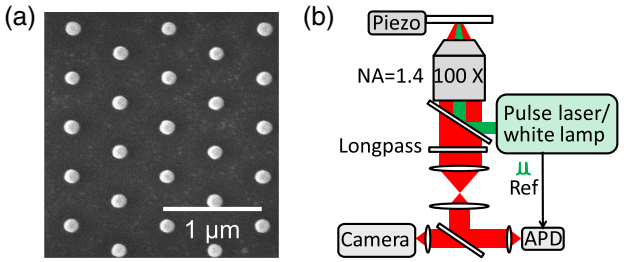

Fig. 2. (a) SEM image of the nanoantenna array. (b) Schematic of the setup.

localization, the laser is focused on the back focal plane of the objective so that an area with a diameter of ~30 μm on the sample is illuminated and the image of fluorescence is recorded with a CCD camera. The reflection of the array is measured with the same detection path by illuminating the sample with a halogen lamp so that the position of the nanoprobes and the array can be accurately correlated. It is essential that fluorescence and reflection are measured using the same filter and beam-splitter set in the transmission path, to avoid the ~50 nm image shifts that are associated with unavoidable filter wedging. To this end, we use a Nikon microscope with two filter turrets stacked above each other. The green laser light is reflected into the microscope off a dichroic filter in the upper cube. White light is inserted via a regular 50/50 beam splitter in the lower filter cube that also contains a long-pass filter to suppress the laser light. Subsequent to localization, we switch to confocal mode, focusing the laser to a diffraction limited spot. The fluorescence lifetime is measured on individual nanoprobes with an avalanche photodiode (APD) based on time-correlated single-photon counting, where piezos are used for sample position scanning.

Figure 3(a) shows examples of fluorescence and reflection images of the sample. The nanoprobes are identified as diffraction limited peaks in the fluorescence image. The nanoprobes appear to have different intensities mainly due to the inhomogeneity of the excitation spot, which is bright in the center and contains speckles. Meanwhile, the different dye doping in the probes as well as the influence of the array on the excitation, quantum yield, and detection efficiency can also contribute to the variation. However, absolute intensity (as long as the required SNR is reached) does not affect the imaged variable, i.e., lifetime, which is uniform across probes to within 7% in absence of plasmonics. The position of each nanoprobe ($\boldsymbol{r}_{\text{probe}}$) is determined by fitting its fluorescence image with a 2D Gaussian function ($I(\boldsymbol{r}) = I_0 e^{-(\boldsymbol{r}-\boldsymbol{r}_{\text{probe}})^2/2s^2}$) assuming Poisson noise. An area within 250 nm of the center of each peak is selected for the fit. The uncertainty of the position determination can be calculated according to Ref. [54] [Eq. (14)] as ~20 nm, given our photon budget, i.e., given the acquisition time that we choose. Since the radius of the nanoprobes is 20 nm, in this experiment there is no need to collect more counts. The resolution could be improved by using smaller probes. Since the same shot-noise localization limits apply as for PALM and STORM, however, also the number of acquired photons per nanoprobe would need to be increased. We note that at targeted resolutions of a few nanometers, the plasmonic structures might cause systematic localization artifacts, as studied by [53,57], since, for instance, scattered light may appear to be radiated by antennas, not probes. There is a small probability for nanoprobes to be separated by less than the diffraction limit, in which case localization would be inaccurate. Based on density, we estimate at most 3% of our measurement points to be affected, and likely less, since we discard those nanoprobes whose fluorescence images are larger than the diffraction limit. This potential problem can be further reduced by diluting the probes.

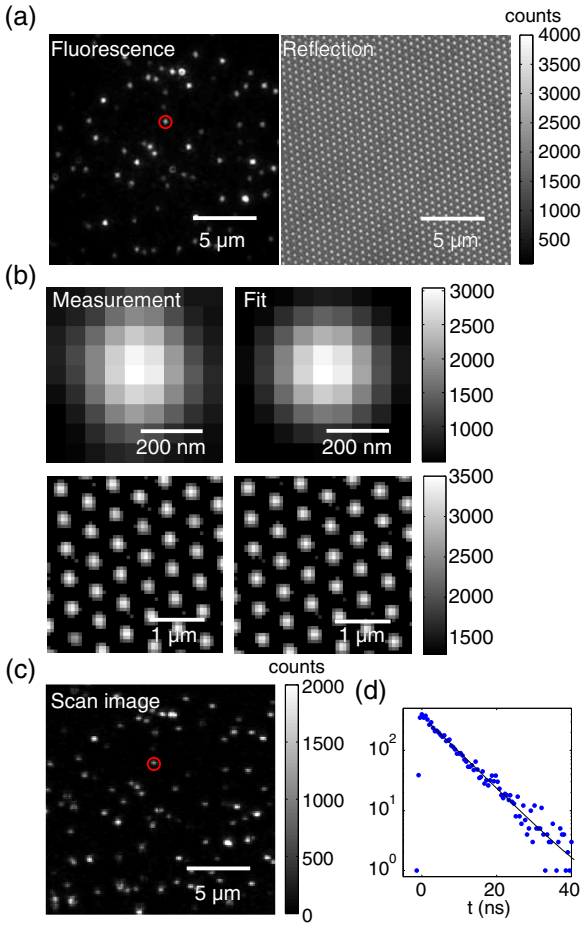

Fig. 3. (a) Measured images of (left) fluorescence and (right) reflection from the same area of the sample. (b) Measured (top left) fluorescence image from the nanoprobe marked with a red circle in (a) and (bottom left) reflection image from vicinity nanoantennas compared to (right) their fits. (c) The scan image corresponding to (a). (d) Measured decay histogram of the nanoprobe marked by the red circles in (a) and (c) and the single exponential fit to it.

The hexagonal array of nanoantennas is clearly resolved in the reflection image in Fig. 3(a). Prior to probe deposition, the nanoantennas look highly uniform in brightness. Once probes are deposited, approximately 10% of antennas appear slightly dimmer, which we attribute to a slight modification of antenna scattering due to the dielectric perturbation formed by a probe. The positions of the Al nanoantennas near the nanoprobes are determined by fitting the reflection image with a sum of 2D Gaussian functions arranged in a hexagonal array. An area of about 3 μm × 3 μm around each nanoprobe is selected to determine the position of the nearest Al particle to the nanoprobe, which we define as the origin of the unit cell. We note that white-light imaging of a periodic structure is not trivial due to the Talbot effect [58], which causes additional image features. We found that the robustness of the fit procedure can be improved by suppressing the Talbot effect in the data simply by ignoring all pixels that are below 50% of the image maximum. Figure 3(b) shows an example of the fractions of fluorescence and reflection images used to determine the position of a nanoprobe and the corresponding images of the fit results. The precision of the localization of the nanoantennas has similar dependence on the SNR and total number of counts. Due to the larger fitting area, the error is only about 7 nm and is negligible compared with the size of the nanoprobes. Finally, the position of the nanoprobes is translated into a quarter of the primitive cell of the hexagonal array defined by the boundaries of the primitive cell and the symmetry axes, as illustrated in Fig. 1(a).

The LDOS of each nanoprobe is proportional to the total decay rate of electromagnetic channels, including both the radiative

decay and quenching in the metallic nanoparticles [59,60]. Considering the existence of intrinsic nonradiative decay channels that are unaffected by the array, the enhancement of LDOS (η_{LDOS}) can be determined from the fluorescent lifetime according to the relation

$$\eta_{\mathrm{LDOS}}(\boldsymbol{r}) = \left(\frac{1}{\tau(\boldsymbol{r})} - \gamma^0_{\mathrm{non}}\right)\cdot\frac{1}{\gamma^0_r} = \left(\frac{1}{\tau(\boldsymbol{r})} - (1-\mathrm{QY}^0)\frac{1}{\tau^0}\right)\cdot\frac{\tau^0}{\mathrm{QY}^0}, \quad (2)$$

where γ^0_r and γ^0_{non} are the intrinsic radiative and nonradiative decay rates of the nanoprobes, and QY^0 is the intrinsic quantum yield. The superscript 0 indicates the environment of the reference, i.e., dye molecules embedded in polystyrene spheres on a glass substrate without influence from the nanoantenna array. Apart from lifetime, enhancement of the fluorescence intensity has also been used to characterize the LDOS. The disadvantage of using intensity as a measure for LDOS, however, is that intensity is the convoluted result of local pump field enhancement, LDOS enhancement, quenching, probe-to-probe variations, and quenching during the measurement procedure. Therefore, here we choose the fluorescence lifetime to determine the LDOS of plasmonic antenna systems.

To measure the fluorescent lifetime (τ) of individual nanoprobes, we focus the laser on the sample and scan the sample position so that only one nanoprobe is excited in each measurement. Figure 3(c) shows an example of the fluorescence intensity detected by the APD as a function of sample position obtained from such a confocal scan, which corresponds well with the camera image in Fig. 3(a). The apparent mismatch between probe intensities detected in camera image and the scan image is due to the different excitation methods, i.e., inhomogeneous collimated illumination, versus focused illumination at constant power. The lifetime of each nanoprobe is obtained by fitting a single exponential function to the decay histogram obtained for the pixels corresponding to each probe in the confocal lifetime scan. Figure 3(d) shows an example of the decay histogram and the fit for the nanoprobe marked with red circles in Figs. 3(a) and 3(c).

Repeating the measurements on 1044 different nanoprobes, we obtain the fluorescence lifetime as a function of position, as shown in Fig. 4. The fluorescence lifetime shows a clear dependence on probe position. The lifetime is low in the region close to the Al nanoantenna, which agrees with the fact that the electrical field intensity is usually much higher in this regime due to the LSPRs. The lifetime increases with the increasing distance from the nanoantenna and slightly decreases near the boundaries of the primitive cell. As regards the spatial distribution of sampling points, we note that almost no nanoprobe is detected at the position of the nanoantenna (consider a 20 nm uncertainty in the position accuracy and the nanoantenna size), while the density of the nanoprobes is large at the particle edge. This could be due to the fact that any nanoprobes that are deposited on top of the nanoantennas tend to aggregate at the nanoantenna base during the drying process.

To convert the random cloud of sampling points into a map of lifetime, we divide the quarter of the primitive cell into a square grid with a pixel size of 10 nm, corresponding to $N_{\mathrm{grid}} \sim 650$ grid points. The lifetime at each grid point is determined as the averaged lifetime of nanoprobes within 20 nm of the grid point.

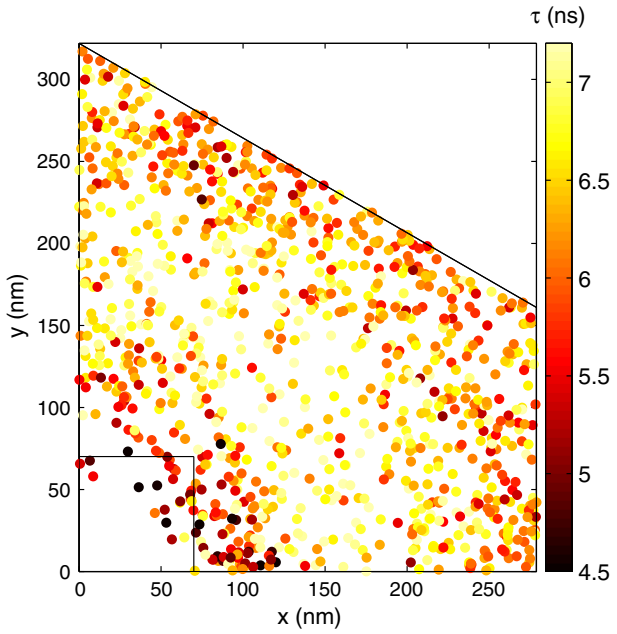

Fig. 4. Measured fluorescence lifetime from 1044 nanoprobes as a function of probe position. Black lines indicate the boundary of the primitive cell and estimated edges of the nanoantenna.

Figure 5(a) shows the map of measured lifetime constructed from the data in Fig. 4, as obtained by averaging the lifetime of all probes in an area ΔA (40 nm across) centered at each pixel (pixel spacing 10 nm), as per the example discussed in Section 2. This representation brings out more clearly than the scatter plot that the lifetime is suppressed to below 5.5 ns within 20 nm from the particles, while it is above 6.6 ns farther away from the particles. To convert measured lifetime data in an LDOS map, one requires a reference lifetime measurement, as well as a quantum yield estimate for the emitters. To obtain a reference, the lifetime of 28 nanoprobes deposited on a substrate without plasmon particles is measured. As intrinsic lifetime (τ_0) of the nanoprobes,

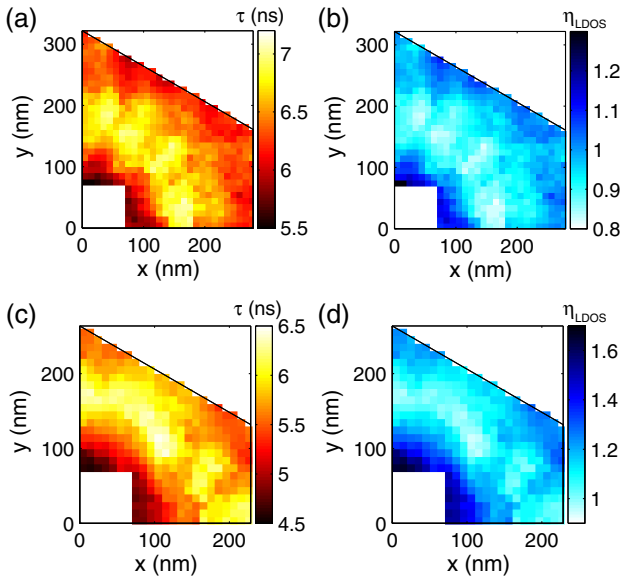

Fig. 5. Constructed map of (a) and (c) fluorescence lifetime and (b) and (d) LDOS. (a) and (b) Pitch = 550 nm. (c) and (d) Pitch = 450 nm.

we find 6.21 ± 0.09 ns. The standard deviation (0.46 ns) shows there is a 7% lifetime variation between different nanoprobes, showing the necessity of averaging multiple probes per pixel. The average lifetime agrees with the results measured by Kwadrin and Koenderink [61], in which the intrinsic radiative and nonradiative decay rates of similar nanoprobes (Invitrogen Fluospheres F8801, same dye but 100 nm size) are determined to be $\gamma_r^0 = 0.10 \pm 0.01$ ns^{-1} and $\gamma_{non}^0 = 0.07 \pm 0.01$ ns^{-1} based on Drexhage's method. Taking the quantum yield from Ref. [61] in combination with our lifetime measurement, we obtain a map of LDOS enhancement in Fig. 5(b).

For the range of positions probed, and given the spatial averaging over the probe size, we obtain an LDOS enhancement variation in the band from 0.85 (slight inhibition when away from the Al nanoparticles) to 1.35 (moderate enhancement near the Al nanoparticles), meaning a total variation by a factor of 1.6. The increase of LDOS near the Al nanoparticles is only moderate compared to other reported LDOS enhancements, which are typically up to ∼20 for single molecule measurements near simple metal particles [2], and of the order of 3 to 5 for nanosized emitters [3]. This can be attributed to the fact that both the thin polymer layer covering the structures and the radius of the nanoprobes we used keep the emitters from entering the ∼10 nm shell around the metal surface where the LSPR are strongest. Also, averaging over the nanoprobe size reduces the apparent LDOS variation, since each nanoprobe contains an ensemble of molecules, thereby biasing our signal toward measuring molecules that are least quenched and, hence, least close to the metal where LDOS is highest. We note that this limitation can be lifted by performing localization microscopy with single emitters rather than nanoprobes (at the price of photon count rate). The fact that emission is inhibited in a ring between the particle and the edge of the primitive cell may appear surprising, but is further confirmed by theory outlined in Section 5.

Similar measurements are done on a nanoantenna array with the same antenna design and a different lattice constant of 450 nm. Figures 5(c) and 5(d) show the maps of measured lifetime and LDOS enhancement obtained from 717 nanoprobes. The LDOS has a similar distribution and in general a slightly larger value compared with that of the array with 550 nm pitch, namely, a large enhancement (∼1.6) near the nanoparticle, slight inhibition or no change away from the nanoparticle and slight enhancement (∼1.2) near the boundary of the primitive cell. This result indicates that the lattice constant of the investigated nanoantenna arrays doesn't significantly influence the LDOS distribution. The LDOS can be slightly increased by reducing the pitch of the nanoantennas.

Finally, we check if the nanoprobes are distributed as we predict from the Monte Carlo experiments by making a histogram of the number of probes per pixel. Figure 6 shows the comparison between the actual distributions of the nanoprobes and the results from Monte Carlo experiments. Here we consider that the nanoprobes have avoided the position of the nanoantennas ($x, y < 60$ nm). The distribution of the nanoprobes for 550 nm pitch agree well with our prediction, which confirms our estimate for the required number of nanoprobes. For 450 nm pitch, the distribution deviates more from the prediction. This can be attributed to the aggregation of the nanoprobes near the edge of the nanoparticles, which becomes more pronounced with the decrease of pitch.

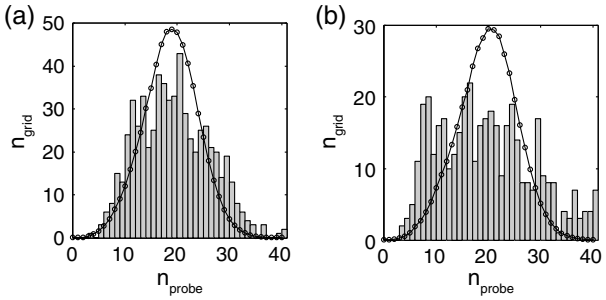

Fig. 6. Histograms plotting the number of grid cells n_{grid} (vertical axis) in the measured spatial map with exactly n_{probe} (horizontal axis) nanoprobes in their averaging areas. Plotted over the histograms from experiment (gray bars) are the results from Monte Carlo experiments (connected dots). (a) Pitch = 550 nm. (b) Pitch = 450 nm.

4. COMPARISON TO NEAR-FIELD LDOS MEASUREMENT

Up to this point, we have introduced a method to map the LDOS of plasmonic nanostructures with stochastic superresolution and realized it on a hexagonal array of Al nanoparticles. The remainder of the paper consists of two parts, namely, interpreting the veracity and quality of the measured LDOS map first on the basis of complementary measurements, and second on the basis of calculations. As a complementary measurement technique with subdiffraction-limited resolution, we have also performed lifetime measurements using an NSOM head mounted on top of the same microscope, as shown in Fig. 7(a). We use the near-field tip as a fluorescence excitation source. The tip is a tapered glass fiber coated with an ∼150 nm Al layer. The end of the tip is polished with focused ion beam milling to form an ∼100 nm aperture [62]. For fluorescence excitation, the green excitation laser is coupled into the cleaved untapered end of the fiber, resulting in a strong electric field confined at the tip aperture. As a source of fluorescence, a 15 nm layer of polystyrene doped with 3 wt. % dye molecules (BASF Lumogen F305) is spin coated on the nanoantenna array, which has absorption and emission spectra similar to that of the nanoprobes. With a standard tuning-fork shear-force feedback loop, the tip is approached to ∼10 nm of the surface of the sample so as to excite the dye molecules with the near field under the aperture (estimated diameter of ≲150 nm). To obtain lifetime data, the lateral (XY) position of the tip is held stationary in the microscope focus, while the same sample scanning piezos are used to scan the sample as in our confocal measurements. In this manner, the fluorescence is collected by the microscope with the intensity and lifetime measured by the APD as function of excitation position on the sample. Meanwhile, the topography of the sample surface is measured according to the shear-force feedback. The scan is operated under a speed of 0.72 μm/s, with the x axis the fast axis and a detection time of 2.5 ms per pixel. We plot only the backward scan direction.

Figures 7(b)–7(d) show maps of topography, fluorescence intensity, and lifetime, respectively, of the dye molecules with the x and y axes parallel with the edges of the nanoantennas. The periodicity of the topography map agrees with the SEM image of the array. The fluorescence intensity varies with the variation in topography, which indicates a good correspondence between the position determined from the topography map and the fluorescence excitation spot. From the topography map we estimate

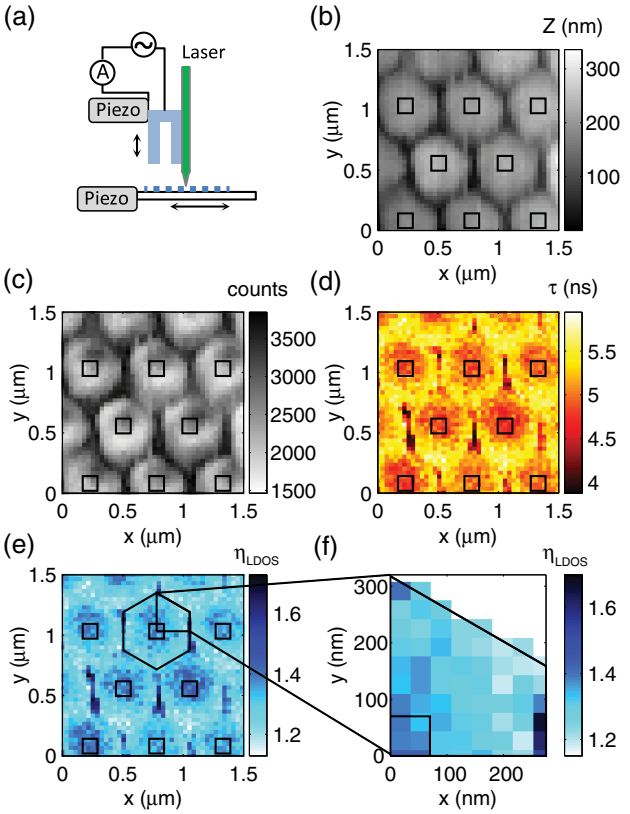

Fig. 7. (a) Schematic of the NSOM head. Measured maps of (b) topography, (c) fluorescence intensity, (d) lifetime, and (e) LDOS enhancement calculated from the measured lifetime. (f) A fraction of (e) representing the LDOS enhancement in a quarter of a primitive cell of the array.

the position of the nanoantennas, as illustrated by the black squares. From the lifetime map, we calculate the LDOS enhancement as a function of the excitation position ($\boldsymbol{r}$) according to Eq. (2) with $\tau^0 = 5.2$ ns the intrinsic lifetime of the dye molecules measured on a similar dye layer on a flat substrate and $QY^0 = 76\%$ the intrinsic quantum yield of the dye molecules in the dye layer measured with an integrating sphere. Figure 7(e) shows the LDOS enhancement obtained from the lifetime map and for direct comparison with Fig. 5(b), we show in Fig. 7(f) a fraction of Fig. 7(e), which represents the LDOS enhancement in a quarter of a primitive cell. The LDOS is high close to the nanoantennas and decreases with increasing distance from the nanoantennas. Along the boundary parallel with the vertical edges of the nanoantennas, there is a sharp increase of LDOS within 2 pixels (~60 nm).

Compared with the stochastic superresolution method introduced in previous sections, the NSOM method also reports an increase of the LDOS near the nanoparticles. However, despite the fact that this measurement uses a state-of-the-art NSOM head and tip, the spatial confinement of the LSPRs that is evident from the superresolution map is lost due to the lower resolution of the NSOM, and the small increase of LDOS near the boundary of the primitive cell is not detected. Moreover, we interpret the sharp LDOS increase along vertical stripes as a topographic artifact. These stripes occur farthest away from the metal particles, and the topography signal shows that they coincide with the tip most closely approaching the dye, as it fits in its entirety in between the metal particles. Crucially, it should be noted that since the tip has a metal coating, it can itself cause LDOS variations that strongly depend on the tip–sample distance [26]. On the other hand, the NSOM method cannot be salvaged by using uncoated tips, as this in itself spoils resolution. All measurements in Fig. 4 require only 20 independent confocal lifetime imaging scans. While in our system each scan took about 30 min, acquisition times could be reduced by, for instance, using a higher repetition rate laser, or performing line-by-line imaging with a streak camera. The NSOM method requires only a single scanning measurement of about the same duration, yet has a large overhead in tip fabrication time.

To sum up, the stochastic superresolution method is (1) easier to operate, (2) superior in resolution, and (3) free from topography artifacts and the influence of the metalized tip, which can introduce significant errors and is, therefore, in all aspects superior to the scanning-excitation technique based on NSOM.

5. ANALYSIS BASED ON FDTD SIMULATION

To validate the comparison of the two experimental methods presented in the previous sections, we have simulated the LDOS near the center of a finite hexagonal array of 300 Al nanopyramids (an area of 11 μm × 11 μm) with a pitch of 550 nm on a glass substrate with the finite-difference time-domain (FDTD) method [63]. An electric dipole of unit dipole moment $\boldsymbol{p}$ is placed at the probe position, 50 nm above the air–glass interface, as a source. The LDOS enhancement is obtained from monitoring the radiated flux out of, and the absorbed power inside, a box enclosing the dipole source and the center nanoantenna of the array, using frequency-domain monitors. The sum of the transmitted and absorbed power gives the total power required to drive the fixed strength source dipole ($P(\boldsymbol{p}, \boldsymbol{r})$), and thereby the LDOS enhancement ($\eta^{\boldsymbol{p}}_{\mathrm{LDOS}}(\boldsymbol{p}, \boldsymbol{r})$) can be calculated as

$$\eta^{\boldsymbol{p}}_{\mathrm{LDOS}}(\boldsymbol{p}, \boldsymbol{r}) = \frac{P(\boldsymbol{p}, \boldsymbol{r})}{P_0(\boldsymbol{p})}, \tag{3}$$

with $P_0(\boldsymbol{p})$ the radiative power of dipole $\boldsymbol{p}$ at the same height above a glass substrate. Assuming that the dye molecules are randomly oriented in the nanoprobes, we calculate the average LDOS enhancement of dye molecules in a nanoprobe by averaging over three orthogonal dipole orientations [64].

Figure 8(a) shows the simulated average LDOS enhancement in a quarter of a primitive cell in the center of the array. The result agrees well with the result measured from the stochastic superresolution method (Fig. 5), i.e., the LDOS enhancement is large (more than 1.5) near the Al nanoparticle, decreases immediately to about 0.8 as the dipole moves away from the Al nanoparticle, and slightly increases to about 1.3 near the boundary of the primitive cell. There is a large gradient of the LDOS near the Al nanoparticles as expected, which is not accessible in the experiment due to the finite radius of the probes. At positions away from the Al nanoparticles, the measurement results agree well both qualitatively and quantitatively with the simulation (5% to 10% error, with all major features reproduced). We note that the absence of dielectric encapsulation of the source in FDTD is expected to have little influence on the result. Previous studies on photonic crystals and layered systems have shown that dielectric encapsulation of LDOS probes only introduces a multiplicative local field factor and has almost no effect on the LDOS

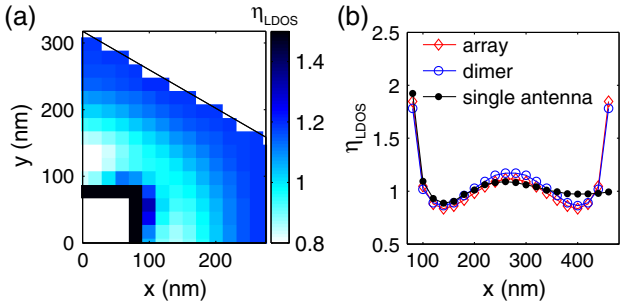

Fig. 8. (a) Simulated map of LDOS enhancement of a hexagonal array with a pitch of 550 nm. Corresponding measurement result is shown in Fig. 5(b). (b) Comparison of simulated LDOS enhancements of an array and a dimer.

distribution [65–67]. While the correspondence between superresolution measurement and FDTD results is good, the result measured with NSOM markedly differs. This furthermore validates that the stochastic superresolution method has overwhelming advantages over the scanning-excitation technique based on NSOM, in particular because it avoids topographic artifacts and the large influence of the tip itself on the LDOS.

Finally, aside from the pure methodological point of view of superresolution LDOS mapping, one can also wonder what physically determines the LDOS distribution. While the LDOS distribution near single metal nanoparticles is well understood, for instance, from Mie calculations [68], in periodic plasmon particle systems it is not. We investigated the origin of the LDOS distribution based on further FDTD simulations. The LDOS can be hypothesized to be modified by the antenna array through three distinct mechanisms: LSPRs generated by individual nanoantennas, coupling between neighboring nanoantennas, and/or collective lattice modes of the array. To distinguish the contribution of these three possible mechanisms, we compare the LDOS in the lattice with the LDOS introduced by a single nanoantenna, and the LDOS along the axis between a pair of nanoantennas for a dimer with separation equal to the lattice constant of the array. As shown in Fig. 8(b), the LDOS enhancement introduced by the single nanoantenna (black) is high near the edge of the nanoantenna due to the LSPR. As the dipole moves away, the influence of the nanoantenna decreases and the LDOS enhancement starts to oscillate around 1 with a decreasing amplitude. The oscillation can be attributed to the interference of the dipole field and its reflection from the substrate at the position of the nanoantenna. Almost the same results are obtained for the array (measurement as well as FDTD result) and the dimer for $x < 200$ nm. As the dipole moves farther, instead of decreasing, the LDOS enhancement continues increasing, resulting in a peak in the middle of two nanoantennas. This is commensurate with the notion that the field reflected off both particles can form a standing wave, given that the particle separation is of the order of a wavelength. Since the blue and red curves for the dimer and a full array, respectively, show the same position dependence, we conclude that the LDOS modification is well captured by a dimer model, without requiring recourse to the lattice modes.

6. CONCLUSION

We have introduced an experimental method to map the local density of states in periodic nanostructures based on stochastic superresolution. This method has been realized on a hexagonal array of Al nanoantennas to map the LDOS enhancement at a wavelength of 605 nm with a resolution of ~40 nm, the result of which agrees with FDTD simulation.

In our implementation we were limited to structures of periodicity exceeding the wavelength, to surface probing, and to moderate (40 nm) resolutions. Already in this limit, the stochastic superresolution method is superior to scanning-excitation NSOM in terms of both simplicity and accuracy. However, the limitations of our method can be easily overcome. This method applies to any nanostructure with repeated units, provided that the nanostructure can be located in a white-light image. If fiducial, isolated markers are added around a structure at fabrication time, they can be used to pinpoint the structure with nanometer accuracy even if the structure itself cannot be resolved due to a subdiffraction pitch. Although the measurement introduced in this article is conducted on the surface of a nanoantenna array, we note that the method is not limited to surface measurements. For example, three-dimensional mapping can be performed by embedding the nanoprobes in a dielectric layer on the nanostructure at different height slices, or by using axial localization techniques [69]. As regards resolution, at the price of photon count rate and, hence, acquisition time, this method could be used with single molecules as probes, thereby allowing 1 order of magnitude resolution improvement.

By using our method for LDOS mapping, we were able to resolve a simple, yet important, question regarding the physics of fluorescence in plasmonic lattices, as we could confirm that LDOS variations are well explained by single-particle properties and nearest-neighbor coupling, without invoking lattice mode physics. We argue that our method extends to many other aspects of photophysics in plasmonic lattices. Indeed, our method applies equally to other optical measurements, such as polarimetry and Fourier imaging [70], thereby allowing us to pinpoint where in the unit cell a source must be placed to obtain optimal brightness, emission polarization, and Purcell factor.

Funding. Stichting voor Fundamenteel Onderzoek der Materie (FOM); Stichting voor de Technische Wetenschappen (STW) (12754).

Acknowledgment. We thank Jaime Gómez Rivas, Dick de Boer, and Henri Jagt for valuable discussions. This work is part of the research programme of the Foundation for Fundamental Research on Matter (FOM), which is part of the Netherlands Organisation for Scientific Research (NWO). This research is supported by the Dutch Technology Foundation STW, which is part of NWO and which is partly funded by the Ministry of Economic Affairs.

REFERENCES

1. P. Anger, P. Bharadwaj, and L. Novotny, "Enhancement and quenching of single-molecule fluorescence," Phys. Rev. Lett. **96**, 113002 (2006).
2. S. Kühn, U. Håkanson, L. Rogobete, and V. Sandoghdar, "Enhancement of single-molecule fluorescence using a gold nanoparticle as an optical nanoantenna," Phys. Rev. Lett. **97**, 017402 (2006).
3. S. Schietinger, M. Barth, T. Aichele, and O. Benson, "Plasmon-enhanced single photon emission from a nanoassembled metal-diamond hybrid structure at room temperature," Nano Lett. **9**, 1694–1698 (2009).
4. T. H. Taminiau, F. D. Stefani, F. B. Degerink, and N. F. Van Hulst, "Optical antennas direct single-molecule emission," Nat. Photonics **2**, 234–237 (2008).

5. R. J. Moerland, T. H. Taminiau, L. Novotny, N. F. van Hulst, and L. Kuipers, "Reversible polarization control of single photon emission," Nano Lett. **8**, 606–610 (2008).
6. R. H. Ritchie, "Plasma losses by fast electrons in thin films," Phys. Rev. **106**, 874–881 (1957).
7. L. Novotny and B. Hecht, *Principles of Nano-Optics* (Cambridge University, 2012).
8. P. Mühlschlegel, H.-J. Eisler, O. J. F. Martin, B. Hecht, and D. W. Pohl, "Resonant optical antennas," Science **308**, 1607–1609 (2005).
9. K. H. Cho, J. Y. Kim, D.-G. Choi, K.-J. Lee, J.-H. Choi, and K. C. Choi, "Surface plasmon-waveguide hybrid polymer light-emitting devices using hexagonal Ag dots," Opt. Lett. **37**, 761–763 (2012).
10. G. Lozano, D. J. Louwers, S. R. Rodríguez, S. Murai, O. T. Jansen, M. A. Verschuuren, and J. Gómez Rivas, "Plasmonics for solid-state lighting: enhanced excitation and directional emission of highly efficient light sources," Light Sci. Appl. **2**, e66 (2013).
11. G. Lozano, G. Grzela, M. A. Verschuuren, M. Ramezani, and J. Gómez Rivas, "Tailor-made directional emission in nanoimprinted plasmonic-based light-emitting devices," Nanoscale **6**, 9223–9229 (2014).
12. J. Stehr, J. Crewett, F. Schindler, R. Sperling, G. von Plessen, U. Lemmer, J. Lupton, T. Klar, J. Feldmann, A. Holleitner, M. Forster, and U. Scherf, "A low threshold polymer laser based on metallic nanoparticle gratings," Adv. Mater. **15**, 1726–1729 (2003).
13. W. Zhou, M. Dridi, J. Y. Suh, C. H. Kim, D. T. Co, M. R. Wasielewski, G. C. Schatz, and T. W. Odom, "Lasing action in strongly coupled plasmonic nanocavity arrays," Nat. Nanotechnol. **8**, 506–511 (2013).
14. A. H. Schokker and A. F. Koenderink, "Lasing at the band edges of plasmonic lattices," Phys. Rev. B **90**, 155452 (2014).
15. X. Meng, J. Liu, A. V. Kildishev, and V. M. Shalaev, "Highly directional spaser array for the red wavelength region," Laser Photon. Rev. **8**, 896–903 (2014).
16. S. Mokkapati, F. J. Beck, A. Polman, and K. R. Catchpole, "Designing periodic arrays of metal nanoparticles for light-trapping applications in solar cells," Appl. Phys. Lett. **95**, 053115 (2009).
17. R. Chriki, A. Yanai, J. Shappir, and U. Levy, "Enhanced efficiency of thin film solar cells using a shifted dual grating plasmonic structure," Opt. Express **21**, A382–A391 (2013).
18. R. A. Pala, J. White, E. Barnard, J. Liu, and M. L. Brongersma, "Design of plasmonic thin-film solar cells with broadband absorption enhancements," Adv. Mater. **21**, 3504–3509 (2009).
19. V. E. Ferry, L. A. Sweatlock, D. Pacifici, and H. A. Atwater, "Plasmonic nanostructure design for efficient light coupling into solar cells," Nano Lett. **8**, 4391–4397 (2008).
20. F. Le, D. W. Brandl, Y. A. Urzhumov, H. Wang, J. Kundu, N. J. Halas, J. Aizpurua, and P. Nordlander, "Metallic nanoparticle arrays: A common substrate for both surface-enhanced Raman scattering and surface-enhanced infrared absorption," ACS Nano **2**, 707–718 (2008).
21. P. Kühler, M. Weber, and T. Lohmüller, "Plasmonic nanoantenna arrays for surface-enhanced Raman spectroscopy of lipid molecules embedded in a bilayer membrane," ACS Appl. Mater. Interfaces **6**, 8947–8952 (2014).
22. L. Billot, M. L. de la Chapelle, A.-S. Grimault, A. Vial, D. Barchiesi, J.-L. Bijeon, P.-M. Adam, and P. Royer, "Surface enhanced Raman scattering on gold nanowire arrays: evidence of strong multipolar surface plasmon resonance enhancement," Chem. Phys. Lett. **422**, 303–307 (2006).
23. N. Félidj, J. Aubard, G. Lévi, J. R. Krenn, M. Salerno, G. Schider, B. Lamprecht, A. Leitner, and F. R. Aussenegg, "Controlling the optical response of regular arrays of gold particles for surface-enhanced Raman scattering," Phys. Rev. B **65**, 075419 (2002).
24. V. G. Kravets, F. Schedin, A. V. Kabashin, and A. N. Grigorenko, "Sensitivity of collective plasmon modes of gold nanoresonators to local environment," Opt. Lett. **35**, 956–958 (2010).
25. P. Offermans, M. C. Schaafsma, S. R. K. Rodríguez, Y. Zhang, M. Crego-Calama, S. H. Brongersma, and J. Gómez Rivas, "Universal scaling of the figure of merit of plasmonic sensors," ACS Nano **5**, 5151–5157 (2011).
26. W. P. Ambrose, P. M. Goodwin, R. A. Keller, and J. C. Martin, "Alterations of single molecule fluorescence lifetimes in near-field optical microscopy," Science **265**, 364–367 (1994).
27. M. Frimmer, Y. Chen, and A. F. Koenderink, "Scanning emitter lifetime imaging microscopy for spontaneous emission control," Phys. Rev. Lett. **107**, 123602 (2011).
28. J. P. Hoogenboom, G. Sanchez-Mosteiro, G. Colas des Francs, D. Heinis, G. Legay, A. Dereux, and N. F. van Hulst, "The single molecule probe: nanoscale vectorial mapping of photonic mode density in a metal nanocavity," Nano Lett. **9**, 1189–1195 (2009).
29. V. Krachmalnicoff, E. Castanié, Y. De Wilde, and R. Carminati, "Fluctuations of the local density of states probe localized surface plasmons on disordered metal films," Phys. Rev. Lett. **105**, 183901 (2010).
30. M. A. Lieb, J. M. Zavislan, and L. Novotny, "Single-molecule orientations determined by direct emission pattern imaging," J. Opt. Soc. Am. B **21**, 1210–1215 (2004).
31. D. W. Pohl, W. Denk, and M. Lanz, "Optical stethoscopy: image recording with resolution $\lambda/20$," Appl. Phys. Lett. **44**, 651 (1984).
32. J. Michaelis, C. Hettich, J. Mlynek, and V. Sandoghdar, "Optical microscopy using a single-molecule light source," Nature **405**, 325–328 (2000).
33. L. Aigouy, Y. D. Wilde, and M. Mortier, "Local optical imaging of nanoholes using a single fluorescent rare-earth-doped glass particle as a probe," Appl. Phys. Lett. **83**, 147–149 (2003).
34. S. Kühn, C. Hettich, C. Schmitt, J.-P. Poizat, and V. Sandoghdar, "Diamond colour centres as a nanoscopic light source for scanning near-field optical microscopy," J. Microsc. **202**, 2–6 (2001).
35. Y. Sonnefraud, N. Chevalier, J.-F. Motte, S. Huant, P. Reiss, J. Bleuse, F. Chandezon, M. T. Burnett, W. Ding, and S. A. Maier, "Near-field optical imaging with a CdSe single nanocrystal-based active tip," Opt. Express **14**, 10596–10602 (2006).
36. H. Gersen, M. F. García-Parajó, L. Novotny, J. A. Veerman, L. Kuipers, and N. F. van Hulst, "Influencing the angular emission of a single molecule," Phys. Rev. Lett. **85**, 5312–5315 (2000).
37. A. Cuche, O. Mollet, A. Drezet, and S. Huant, "Deterministic quantum plasmonics," Nano Lett. **10**, 4566–4570 (2010).
38. V. Krachmalnicoff, D. Cao, A. Cazé, E. Castanié, R. Pierrat, N. Bardou, S. Collin, R. Carminati, and Y. D. Wilde, "Towards a full characterization of a plasmonic nanostructure with a fluorescent near-field probe," Opt. Express **21**, 11536–11545 (2013).
39. R. Beams, D. Smith, T. W. Johnson, S.-H. Oh, L. Novotny, and A. N. Vamivakas, "Nanoscale fluorescence lifetime imaging of an optical antenna with a single diamond NV center," Nano Lett. **13**, 3807–3811 (2013).
40. A. G. Curto, G. Volpe, T. H. Taminiau, M. P. Kreuzer, R. Quidant, and N. F. van Hulst, "Unidirectional emission of a quantum dot coupled to a nanoantenna," Science **329**, 930–933 (2010).
41. D. M. Koller, U. Hohenester, A. Hohenau, H. Ditlbacher, F. Reil, N. Galler, F. R. Aussenegg, A. Leitner, A. Trügler, and J. R. Krenn, "Superresolution moiré mapping of particle plasmon modes," Phys. Rev. Lett. **104**, 143901 (2010).
42. A. Huck, S. Kumar, A. Shakoor, and U. L. Andersen, "Controlled coupling of a single nitrogen-vacancy center to a silver nanowire," Phys. Rev. Lett. **106**, 096801 (2011).
43. T. van der Sar, E. C. Heeres, G. M. Dmochowski, G. de Lange, L. Robledo, T. H. Oosterkamp, and R. Hanson, "Nanopositioning of a diamond nanocrystal containing a single nitrogen-vacancy defect center," Appl. Phys. Lett. **94**, 173104 (2009).
44. S. Kumar, A. Huck, and U. L. Andersen, "Efficient coupling of a single diamond color center to propagating plasmonic gap modes," Nano Lett. **13**, 1221–1225 (2013).
45. E. Betzig, G. H. Patterson, R. Sougrat, O. W. Lindwasser, S. Olenych, J. S. Bonifacino, M. W. Davidson, J. Lippincott-Schwartz, and H. F. Hess, "Imaging intracellular fluorescent proteins at nanometer resolution," Science **313**, 1642–1645 (2006).
46. S. T. Hess, T. P. Girirajan, and M. D. Mason, "Ultra-high resolution imaging by fluorescence photoactivation localization microscopy," Biophys. J. **91**, 4258–4272 (2006).
47. M. J. Rust, M. Bates, and X. Zhuang, "Sub-diffraction-limit imaging by stochastic optical reconstruction microscopy (STORM)," Nat. Methods **3**, 793–796 (2006).
48. H. Lin, S. P. Centeno, L. Su, B. Kenens, S. Rocha, M. Sliwa, J. Hofkens, and H. Uji-i, "Mapping of surface-enhanced fluorescence on metal nanoparticles using super-resolution photoactivation localization microscopy," Chem. Phys. Chem. **13**, 973–981 (2012).
49. H. Cang, A. Labno, C. Lu, X. Yin, M. Liu, C. Gladden, Y. Liu, and X. Zhang, "Probing the electromagnetic field of a 15-nanometre hotspot by single molecule imaging," Nature **469**, 385–388 (2011).

50. L. Wei, C. Liu, B. Chen, P. Zhou, H. Li, L. Xiao, and E. S. Yeung, "Probing single-molecule fluorescence spectral modulation within individual hotspots with subdiffraction-limit image resolution," Anal. Chem. **85**, 3789–3793 (2013).
51. C. Ropp, Z. Cummins, S. Nah, J. T. Fourkas, B. Shapiro, and E. Waks, "Nanoscale probing of image-dipole interactions in a metallic nanostructure," Nat. Commun. **6**, 6558 (2015).
52. Y. V. Miklyaev, S. A. Asselborn, K. A. Zaytsev, and M. Y. Darscht, "Superresolution microscopy in far-field by near-field optical random mapping nanoscopy," Appl. Phys. Lett. **105**, 113103 (2014).
53. E. Wertz, B. P. Isaacoff, J. D. Flynn, and J. S. Biteen, "Single-molecule super-resolution microscopy reveals how light couples to a plasmonic nanoantenna on the nanometer scale," Nano Lett. **15**, 2662–2670 (2015).
54. R. E. Thompson, D. R. Larson, and W. W. Webb, "Precise nanometer localization analysis for individual fluorescent probes," Biophys. J. **82**, 2775–2783 (2002).
55. M. A. Verschuuren, "Substrate conformal imprint lithography for nanophotonics," Ph.D. thesis (Utrecht University, 2010).
56. S. R. K. Rodriguez, F. B. Arango, T. P. Steinbusch, M. A. Verschuuren, A. F. Koenderink, and J. Gómez Rivas, "Breaking the symmetry of forward-backward light emission with localized and collective magnetoelectric resonances in arrays of pyramid-shaped aluminum nanoparticles," Phys. Rev. Lett. **113**, 247401 (2014).
57. K. L. Blythe, E. J. Titus, and K. A. Willets, "Comparing the accuracy of reconstructed image size in super-resolution imaging of fluorophore-labeled gold nanorods using different fit models," J. Phys. Chem. C **119**, 19333–19343 (2015).
58. H. F. Talbot, "LXXVI. Facts relating to optical science. No. IV," Philos. Mag. Ser. 3 **9**, 401–407 (1836).
59. K. Joulain, R. Carminati, J.-P. Mulet, and J.-J. Greffet, "Definition and measurement of the local density of electromagnetic states close to an interface," Phys. Rev. B **68**, 245405 (2003).
60. P. Bharadwaj, B. Deutsch, and L. Novotny, "Optical antennas," Adv. Opt. Photon. **1**, 438–483 (2009).
61. A. Kwadrin and A. F. Koenderink, "Gray-tone lithography implementation of Drexhage's method for calibrating radiative and nonradiative decay constants of fluorophores," J. Phys. Chem. C **116**, 16666–16673 (2012).
62. J. A. Veerman, A. M. Otter, L. Kuipers, and N. F. van Hulst, "High definition aperture probes for near-field optical microscopy fabricated by focused ion beam milling," Appl. Phys. Lett. **72**, 3115 (1998).
63. "FDTD solutions," Lumerical, https://www.lumerical.com/tcad-products/fdtd/.
64. W. L. Vos, A. F. Koenderink, and I. S. Nikolaev, "Orientation-dependent spontaneous emission rates of a two-level quantum emitter in any nanophotonic environment," Phys. Rev. A **80**, 053802 (2009).
65. I. S. Nikolaev, W. L. Vos, and A. F. Koenderink, "Accurate calculation of the local density of optical states in inverse-opal photonic crystals," J. Opt. Soc. Am. B **26**, 987–997 (2009).
66. F. A. Inam, T. Gaebel, C. Bradac, L. Stewart, M. J. Withford, J. R. Rabeau, and M. J. Steel, "Modification of spontaneous emission from nanodiamond colour centres on a structured surface," New J. Phys. **13**, 073012 (2011).
67. A. Mohtashami and A. F. Koenderink, "Suitability of nanodiamond nitrogen-vacancy centers for spontaneous emission control experiments," New J. Phys. **15**, 043017 (2013).
68. H. Mertens, A. F. Koenderink, and A. Polman, "Plasmon-enhanced luminescence near noble-metal nanospheres: comparison of exact theory and an improved Gersten and Nitzan model," Phys. Rev. B **76**, 115123 (2007).
69. B. Huang, W. Wang, M. Bates, and X. Zhuang, "Three-dimensional super-resolution imaging by stochastic optical reconstruction microscopy," Science **319**, 810–813 (2008).
70. C. I. Osorio, A. Mohtashami, and A. F. Koenderink, "K-space polarimetry of bullseye plasmon antennas," Sci. Rep. **5**, 9966 (2015).